ACS APPLIED MATERIALS & INTERFACES

Research Article

www.acsami.org

Hierarchical $Co_3O_4/Co(OH)_2$ Nanoflakes as a Supercapacitor Electrode: Experimental and Semi-Empirical Model

Mohammad Qorbani,[†] Naimeh Naseri,[†,‡] and Alireza Z. Moshfegh*[,†,§]

[†]Department of Physics, Sharif University of Technology, Tehran 11155-9161, Iran

[‡]School of Physics, Institute for Research in Fundamental Sciences (IPM), Tehran 19395-5531, Iran

[§]Institute for Nanoscience and Nanotechnology, Sharif University of Technology, Tehran 14588-89694, Iran

Supporting Information

ABSTRACT: In this research, facile and low cost synthesis methods, electrodeposition at constant current density and anodization at various applied voltages, were used to produce hierarchical cobalt oxide/hydroxide nanoflakes on top of porous anodized cobalt layer. The maximum electrochemical capacitance of 601 mF cm^{-2} at scan rate of 2 mV s^{-1} was achieved for 30 V optimized anodization applied voltage with high stability. Morphology and surface chemical composition were determined by scanning electron microscopy (SEM) and X-ray photoelectron spectroscopy (XPS) analysis. The size, thickness, and density of nanoflakes, as well as length of the porous anodized Co layer were measured about 460 ± 45 nm, 52 ± 5 nm, 22 ± 3 μm^{-2}, and 3.4 ± 0.3 μm for the optimized anodization voltage, respectively. Moreover, the effect of anodization voltage on the resulting supercapacitance was modeled by using the Butler–Volmer formalism. The behavior of the modeled capacitance in different anodization voltages was in good agreement with the measured experimental data, and it was found that the role and contribution of the porous morphology was more decisive than structure of nanoflakes in the supercapacitance application.

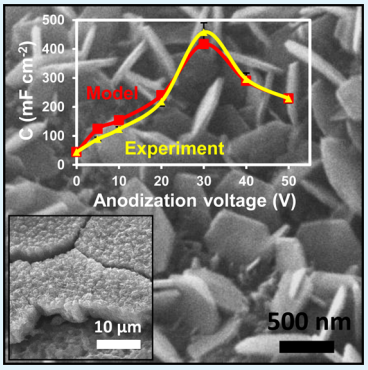

KEYWORDS: *cobalt oxide/hydroxide, anodization, nanoflakes, supercapacitor electrode, modeled capacitance*

1. INTRODUCTION

Energy production and storage are the most important issues for human's today economy and industry. The most promising source of clean energy is sunlight acting in a sustainable way. Examples include conversion of solar energy into chemical energy by generation of hydrogen fuel[1,2] and electricity by photovoltaic devices.[3,4] On the other hand, the energy storage devices, such as rechargeable small-sized ion batteries[5,6] and supercapacitors (SCs),[7−9] are extremely being investigated in past decade. SCs can store energy on the basis of both charge accumulation (e.g., carbon base materials) and reversible Faradaic reactions (e.g., metal oxides) on the surface.[10−12] The former is called electric double layer capacitor (EDLC), and the latter is named as pseudocapacitor. SCs have higher power density and faster charge/discharge rate as compared with conventional batteries.[13,14] However, a lower amount of energy storage in SCs and their lifetimes in comparison with rechargeable batteries are two key challenges for scientists.

Researchers are trying to increase the energy storage (i.e., capacitance and working voltage) and lifetime and, simultaneously, decrease the price of these kinds of capacitors. To achieve these targets, materials, such as ruthenium(IV) oxide,[15] manganese dioxide,[16,17] cobalt oxide/hydroxide,[18−20] nickel(II) oxide/hydroxide,[21−23] FeOOH,[24] $FeCo_2O_4$,[25] $CoNi_2O_4$,[26] Ni_3S_4/Co_3S_4,[27] and $CoNi_2S_4$,[28] have been employed as supercapacitors in the past few years.[29] Among them cobalt oxide/hydroxide has maximum theoretical pseudocapacitance of about 3500 F g^{-1}.[30−32] Supporting Information Table S1 shows a summary review of the most cited papers on cobalt oxide/hydroxide nanostructured materials synthesized by different methods that have been published in past decade. As shown in the table, various nanostructured shapes (mesoporous, nanoflakes, nanotubes, nanowires, and etc.) have been synthesized and their electrochemical characteristics were investigated by different researchers in this period. However, despite several published works on pure theoretical semi-empirical aspects of supercapacitors;[33−36] there is no theoretical model on the effect of morphology on the electrochemical capacitance of the nanostructured cobalt oxide/hydroxide systems.

Recently, self-organized cobalt oxide nanoporous thin film has been grown on cobalt (Co) foil by anodization method by Schmuki's group for the first time.[37] They have overcome the problem of oxygen evolution during the anodization process and have found the optimum conditions for successful anodic growth with high-aspect-ratio ordered nanoporous layers. In here, we have used electrodeposition as a facile and low cost method for formation of cobalt oxide/hydroxide layers

Received: January 30, 2015
Accepted: May 13, 2015
Published: May 13, 2015

DOI: 10.1021/acsami.5b00806
ACS Appl. Mater. Interfaces 2015, 7, 11172−11179

containing nanoflakes on top. Then, the electrodeposited layers were anodized resulted in layers containing nanoflakes on top of the porous structure. The effect of anodization voltages on the surface morphologies, chemical compositions and the resulting electrochemical capacitances are all measured and modeled. The proposed semi-empirical model described experimental observations as well as the contribution of each part (nanoflakes and porous anodized layer) in the overall supercapacitance value.

2. EXPERIMENTAL SECTION

2.1. Electrodeposition. Cobalt (Co) layers were electrodeposited on copper (Cu) foil substrates by galvanostat mode using a conventional three-electrode cell configuration and by a galvanostat/potentiostat (Autolab PGSTAT302). The solutions contained 0.5 M $CoCl_2$ (Sigma-Aldrich, > 98%) and 0.5 M H_3BO_3 (Sigma, 99.5%). The applied current density and the growth time were fixed at 28 mA cm^{-2} and 2000 s, respectively. The copper electrodes were etched prior to each experiment using a diluted nitric acid (Merck, 60%) solution for 1 min. The counter and reference electrodes were platinum (99.99% purity, 1.5 × 1.5 cm^2 sheet) and Ag/AgCl. The thickness of all electrodeposited cobalt layers was measured 16 ± 1 μm using SEM images (see Supporting Information, Figure S1).

2.2. Anodization. Porous nanostructures were synthesized by anodizing the electrodeposited cobalt layers under different applied voltages ranging from 5 to 50 V for 7 h. The electrolyte solution contained a mixed ethylene glycol (EG) with glycerol (Gly) solvent (volume ratio of 1 to 3), 2 M deionized (DI) water, and 0.54 M NH_4F. The temperature of electrolyte was reduced to about 6 ± 1 °C by an ice bath to prevent oxygen evolution reactions on the film/electrolyte interface during the growth.[34] Otherwise, the anodized cobalt layers will be dissolved due to anodization at room (or higher) temperature into the electrolyte and disordered structure will be formed (see Supporting Information Figure S2). The geometric surface area of each sample was 0.25 ± 0.02 cm^2.

2.3. Characterizations. The size and morphology of the prepared cobalt oxide/hydroxide films and their surface chemical compositions were characterized by scanning electron microscopy (SEM, TESCAN-VEGA3-SB) and X-ray photoelectron spectroscopy (XPS), using monochromatic AlK_α radiation source (1486.6 eV), respectively. All binding energy values were calibrated by fixing the C (1s) core level to the 285.0 eV. In addition, all of the peaks were deconvoluted using SDP software (version 4.1) with 80% Gaussian−20% Lorentzian peak fitting. The accuracy in binding energy measurements was ±0.1 eV. It must be noted that all samples were characterized by using SEM and XPS just after the initial electrochemical activation step by cyclic voltammetry (100-cycle at 200 mV s^{-1}).

2.4. Electrochemical Measurements. The electrochemical properties of the samples were studied using galvanostat/potentiostat system (Autolab, PGSTAT302) and cyclic voltammetry (CV), chronopotentiometry (CP), and electrochemical impedance spectroscopy (EIS) techniques. Similar to synthesis step, the counter and reference electrodes were platinum (99.99% purity, 1.5 × 1.5 cm^2 sheet) and Ag/AgCl. In addition, 1 M KOH aqueous solution was used as the electrolyte for these experiments. An initial electrochemical activation step had been performed for all working electrodes before collecting data (100-cycle activation at 200 mV s^{-1}).[38] The specific electrochemical capacitances (capacitance per geometric surface area) of the prepared nanostructures were calculated from the recorded CV curves based on the equation

$$C_A = \frac{\int_{V_i}^{V_f} J(V)\,dV}{\nu(V_f - V_i)} \quad (1)$$

where C_A, $J(V)$ and ν are the specific electrochemical capacitance (mF cm^{-2}), current density response (mA cm^{-2}), and scan rate (V s^{-1}), respectively. V_i and V_f represent the initial and final voltages, respectively. The Coulombic efficiency (η) was calculated from the galvanostatic charge/discharge tests by using the relation[39]

$$\eta = \frac{t_d}{t_c} \times 100 \quad (2)$$

where t_c and t_d represent the time of charge and discharge, respectively. The energy density (E) and power density (P) was estimated by the following equations:

$$E = \frac{1}{2} C_A \Delta V^2 \quad (3)$$

$$P = \frac{E}{t_d} \quad (4)$$

ΔV is the potential window. EIS measurements were also carried out by applying an AC voltage with 5 mV amplitude in a frequency range from 0.01 Hz to 100 kHz at 0.5 V applied voltage.

3. RESULTS AND DISCUSSION

3.1. Structure Characterization. As reported by Schmuki's group,[37] in the anodization method, it is essential that the rate of oxide formation by O^{2-} (K_{ox}) must be in equilibrium with the rate of etching of oxide by F^- (K_{diss}) for an ordered porous structure. This condition is occurred at optimum applied voltage, water content, and fluorine concentration, as well as electrolyte temperature.[37,40,41] In here, all these parameters have been optimized by a systematic careful study (see for example Supporting Information Figure S2 and Figure S3). For saving spaces only the effect of anodization voltage on the prepared samples will be reported in the main text. The SEM images of the non-anodized and anodized samples at different applied voltages are shown in Figure 1. It exhibits a uniform structure with interconnected hierarchical nanoflakes, which have anisotropic morphology on the surface.[30,42]

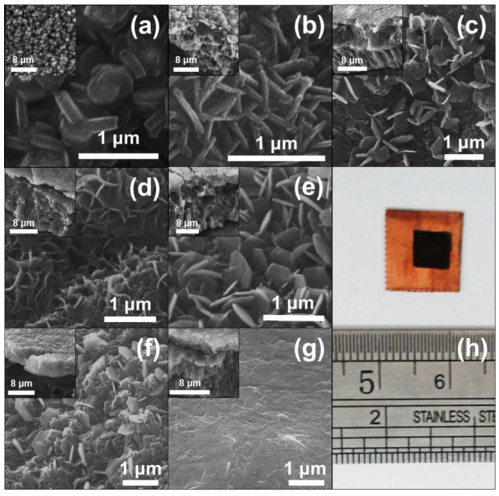

Figure 1. SEM images of the non-anodized (a) and anodized samples at different applied voltages: (b) 5, (c) 10, (d) 20, (e) 30, (f) 40, and (g) 50 V. Inset: Cross section view of the corresponding samples. (h) A typical photograph of a sample.

According to image analysis, the structural parameters of the prepared films were measured and results summarized in Table 1. The density of nanoflakes (n) was estimated about 27 μm^{-2} and 20 μm^{-2} for the non-anodized and anodized samples prepared in range of $10 \leq V \leq 30$ V, respectively. On the basis of our data analysis, it was decreased to about zero by increasing the anodization voltage from 30 to 50 V. The inter

DOI: 10.1021/acsami.5b00806
ACS Appl. Mater. Interfaces 2015, 7, 11172−11179

Table 1. Morphological Characteristics of the Prepared Films

anodization voltage (V)	film thickness l (μm)	flake size d (nm)	flake thickness w (nm)	flake density n (μm^{-2})
0		465 ± 35	133 ± 21	27 ± 4
5	0.9 ± 0.2	410 ± 35	53 ± 6	21 ± 3
10	1.2 ± 0.2	375 ± 30	52 ± 5	19 ± 3
20	2.0 ± 0.3	315 ± 30	49 ± 6	18 ± 3
30	3.4 ± 0.3	460 ± 45	52 ± 5	22 ± 3
40	2.4 ± 0.3	445 ± 45	54 ± 7	13 ± 2
50	2.0 ± 0.3			0

space between nanoflakes is too large (much greater than OH^- ionic radius of 0.110 nm) which can act as an appropriate channel for ion diffusion through the porous layer. Moreover, the thickness of porous anodized layer (l) was increased to 3.4 ± 0.3 μm by increasing the voltage up to 30 V, while, it was decreased to 2.0 ± 0.3 μm by further increasing the anodization voltage to 50 V. The reduction of n and l were attributed to the dissolution of the surface cobalt oxide into the electrolyte by chemical attack of the fluorine (F^-) ions.[40] Hence, the optimum anodization voltage was obtained at 30 V, which led to the thickest porous layer accompanied by uniformly distributed nanoflakes. For higher applied anodization voltages, K_{diss} was found higher than K_{ox} leading to a lower surface area. It is worthy to note that the size of nanoflakes (d) for the sample prepared at 30 V was 460 ± 45 nm, which was the maximum value among all the anodized samples prepared in different voltages. The size of nanoflakes was measured and varied from 300 to 500 nm for all samples. The thickness of the nanoflakes (w) was also about 133 and 50 nm for the non-anodized and anodized samples, respectively (Table 1). The action and presence of F^- ions were responsible for reduction of thickness of the nanoflakes at higher anodization voltage.[43]

It is well established that the morphology of a nanostructure plays an important role for chemical accessibility of OH into the solid porous phase (by controlling the diffusion process), but at the same time, it has to provide the surface with high degree of activity which is crucial in supercapacitance applications.[44] The sample prepared at 30 V applied anodization voltage possessed the maximum surface area. In addition, as the porous layer formed by action of O^{2-} there must be no barrier for diffusion or field-assisted drift of OH^- ions through the solid porous phase. (It will be shown that the reactions are surface controlled.) Therefore, this sample can be considered as an efficient electrode under our experimental condition for supercapacitance applications.

3.2. Surface Chemical Composition. To determine surface chemical composition and oxidation state of the samples, XPS measurements were performed. XPS survey spectrum analysis of the films (see Supporting Information Figure S4) reveals that only Co, O, C, a trace amount of Cl, and metallic Cu presented on the surface. The carbon was originated from the air pollution and/or CO/CO_2 adsorption on the surface of the samples. Figure 2 shows the O (1s) and Co ($2p_{3/2}$) XPS spectra of $[Co_3O_4]_x[Co(OH)_2]_{1-x}$ samples before and after anodization at different applied voltages (10, 30, and 50 V). The O (1s) peaks at 529.9 and 531.2 eV attributed to oxygen in Co_3O_4 and $Co(OH)_2$ compound (Figure 2a). It is obvious that the samples had tendency to shift to $Co(OH)_2$ phase as the applied voltage increased.

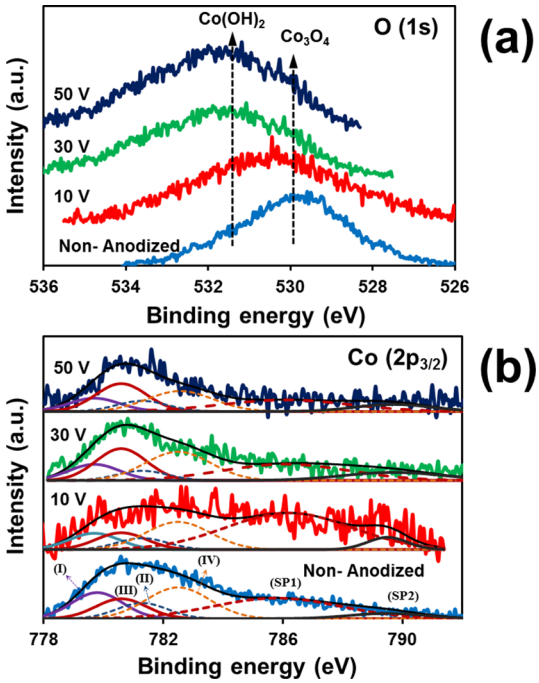

Figure 2. O (1s) (a) and Co ($2p_{3/2}$) core levels (b) XPS spectra of the non-anodized and anodized samples at different voltages. I–IV are correspond to Co_3O_4 phase at 779.8 eV, $Co(OH)_2$ phase at 781.5 eV, asymmetry compensation for cobalt oxide/hydroxide phase 781.3 and 782.3 eV, respectively. Satellite peaks for cobalt hydroxide and cobalt hydroxide is shown by (SP1) and (SP2).

Besides, the Co ($2p_{3/2}$) spectra was deconvoluted to four main peaks were related to[45] (I) Co_3O_4 phase at 779.8 eV, (II) $Co(OH)_2$ phase at 781.5 eV, (III) 781.3 eV, and (IV) 782.3 eV (Figure 2b). The two latter peaks were considered to compensate asymmetry in cobalt oxide/hydroxide phase in deconvolution of Co ($2p_{3/2}$). Two strong satellite features at 786.1 eV or 789.5 are indicative of a film dominated by $Co(OH)_2$ or Co_3O_4 phases, respectively.[45−47] By analysis of the deconvoluted curves, the quantity of x in the $[Co_3O_4]_x[Co(OH)_2]_{1-x}$ was calculated 57 ± 2% for the non-anodized 50 ± 5%, 34 ± 3% and 32 ± 3% for anodized samples at 10, 30, and 50 V, respectively (Supporting Information Figure S5). Hence, the surface composition of the non-anodized sample was $[Co_3O_4]_{0.57}[Co(OH)_2]_{0.43}$ and it transformed to $[Co_3O_4]_{0.32}[Co(OH)_2]_{0.68}$ after applying anodic voltages at 50 V.

3.3. Electrochemical Analysis. Figure 3a shows the typical CV curves of the cobalt oxide/hydroxide nanostructures at the scan rate of 20 mV s^{-1} from −0.1 to 0.55 V potential ranges. Three redox peaks were clearly observed at about 0.08, 0.28, and 0.46 V, which corresponded to the conversion between different cobalt oxidation states according to the following reactions:[30,48−50]

$$Co(OH)_2 + OH^- \rightarrow CoOOH + H_2O + e^- \quad (5)$$

$$Co_3O_4 + H_2O + OH^- \rightarrow 3CoOOH + e^- \quad (6)$$

$$CoOOH + OH^- \rightarrow CoO_2 + H_2O + e^- \quad (7)$$

The presence of cobalt oxide/hydroxide phases shown in CV curves was also verified by our XPS data. It is obvious that the anodic current density of the sample prepared at 30 V applied voltage was higher than the other ones. Hence, this sample

DOI: 10.1021/acsami.5b00806
ACS Appl. Mater. Interfaces 2015, 7, 11172−11179

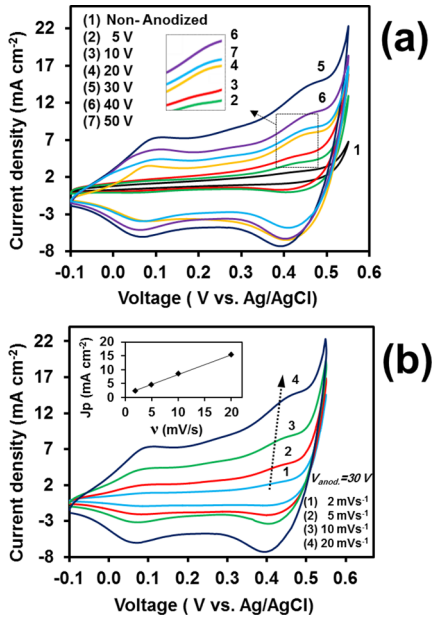

Figure 3. (a) CV curve of the prepared sample at constant scan rate of 20 mV s^{-1} for different anodization voltages and (b) the CV curves of the optimum sample (V^{30V}_{anod}) at different scan rates. Inset: Peak current density of the V^{30V}_{anod} versus scan rate.

exhibited the maximum electrochemical output as a supercapacitor. Besides, the CV curves of this sample were investigated at different scan rates ν (Figure 3b). By increasing ν, the oxidation and reduction peaks shifted continuously to higher and lower potentials, respectively, leading to a larger potential separation between them. The linear behavior in the $J_p-\nu$ diagram implied that the electron transfer processes were surface controlled.[51,52] In addition, it should be noted that the contribution of Cu substrates was negligible (less than 1%) as compared with obtained result.

Figure 4 shows the specific capacitance as a function of anodization voltages and scan rates. The capacitance of the non-anodized sample was measured 44 mF cm^{-2}, and it

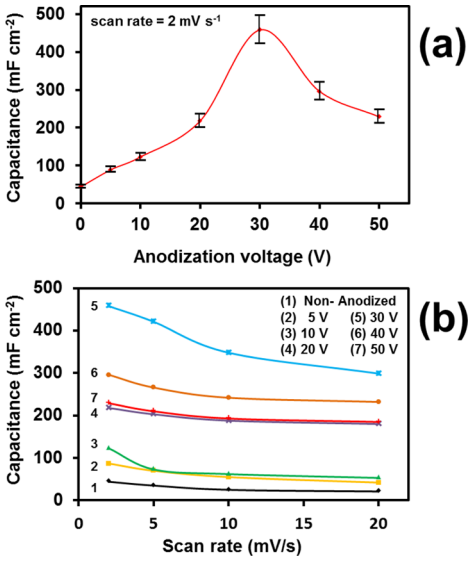

Figure 4. Specific capacitance as a function of the applied anodization voltages (a) and scan rates (b) in different voltages.

reached to a maximum value of 458 mF cm^{-2} for the optimum sample (V^{30V}_{anod}) because of its higher surface area (or higher active mass density of about 2 mg cm^{-2}). Considering Table 1, by increasing the applied voltage to higher than 30 V, the flakes started to disappear, and the thickness of the anodized porous layer was decreased. Subsequently, the capacitance of the films decreased to 229 mF cm^{-2} for the sample anodized at 50 V anodic voltage. Moreover, it should be noted that the capacitance of the V^{30V}_{anod} sample was higher as compared to others for the all scan rates examined in this study (Figure 4b).

The charge/discharge curves of the porous nanoflake $Co_3O_4/Co(OH)_2$ electrodes were evaluated by galvanostatic charge/discharge cycles at a constant current density of 10 mA cm^{-2} in −0.2−0.55 V potential range, which is presented in Figure 5. The slow potential decays in this potential range were

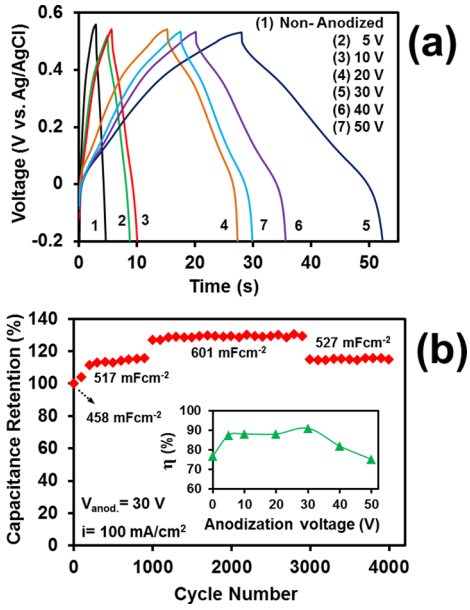

Figure 5. (a) Charge/discharge curves at constant current density 10 mA cm^{-2} and (b) capacitance retention of the optimized sample (30 V applied voltage) as a function of cycle number obtained by galvanostatic charge/discharge mode at 100 mA cm^{-2}. Inset: Coulombic efficiency versus applied anodization voltage.

attributed to surface redox reactions which were in agreement with the result of CV tests.[53] The V^{30V}_{anod} sample had 27.1 ± 0.1 and 25.2 ± 0.1 s charge and discharge time interval acquiring the maximum electrochemical capacitance. The Coulombic efficiency (η) was calculated by charge/discharge curves for each anodization voltage and the result is shown in inset of Figure 5b. η was maximum for the V^{30V}_{anod} sample with 92% and it implied that the surface reactions were reversible as compared to other voltages. The durability of the V^{30V}_{anod} sample was measured by galvanostatic charge/discharge mode for 4000 cycle number (Figure 5b). Capacitance retention was increased to about 126% after 1000 cycles for the optimum sample because of surface chemical activation of the electrode via increasing the contact area between the electrode and the electrolyte during cycling.[29,35] Then, it was highly stable for 2000 cycles with specific electrochemical capacitance value of about 601 mF cm^{-2}. After 3000 cycles, a drop was observed which is because of dissolution of active material by OH^- ions during cycling at the interface of porous layer and compact solid phase (see Supporting Information Figure S6). Besides,

DOI: 10.1021/acsami.5b00806
ACS Appl. Mater. Interfaces 2015, 7, 11172−11179

the energy density and power density of the V_{anod}^{30V} sample was obtained at about 0.4 Wh m^{-2} and 56 W m^{-2} at current density of 10 mA cm^{-2}, respectively. The energy density was reduced to about 35% of the first value when electrode worked at 10 times higher power density (see Supporting Information Figure S7). Further, the performance of this sample will be lower than expected when they will be used in a full device.[54]

Figure 6a shows Nyquist plots of the non-anodized and anodized samples exhibit a typical semicircle at tested frequency

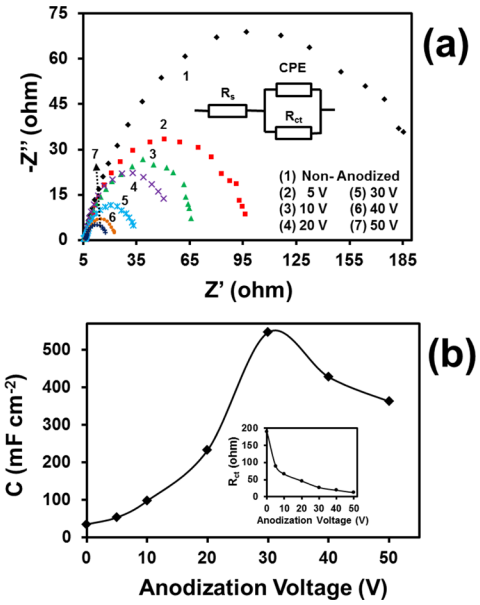

Figure 6. (a) Nyquist plots of non-anodized and anodized samples. The inset is the equivalent circuit. (b) The fitted normalized capacitances and charge transfer resistances versus applied anodization voltage. The geometric surface area of each sample was 0.25 ± 0.02 cm^2.

region. The average values of the ohmic resistance of the electrolytes and cell components (R_s) was 6.1 ± 0.1 Ω. Meanwhile, the semicircle corresponds to parallel RC elements, the charge transfer resistance (R_{ct}), and the constant phase capacitance (CPE).[55] The radii of the semicircles were decreased by increasing the applied voltage indicating better charge transfer process for higher anodization voltages. The fitted values of the capacitances and R_{ct} are shown in Figure 6b. The behavior of the fitted capacitance (CPE constant was 0.85 ± 0.02) which was obtained by EIS experiment showing a good agreement with the electrochemical data. The smallest and highest normalized capacitance of about 35 and 546 mF cm^{-2} were obtained (by EIS analysis) for the non-anodized and V_{anod}^{30V} samples, respectively.

4. SEMI-EMPIRICAL MODELING

For further understanding the nature and physics of optimized supercapacitance, we have used a semi-empirical model. Figure 7 shows schematic representation of the nanostructured layers. The following assumptions were made in this model: (1) Only faradaic reactions occurred and double layer charging was ignored as a result of EIS fitting. (2) Both Co_3O_4 and $Co(OH)_2$ composition had about the same electrochemical capacitance (their theoretical capacitances are about ∼3500 F g^{-1}).[30−32] (3) No charge carrier accumulation occurred on the solid phase because the rate-determining step (RDS) is the OH^- ion

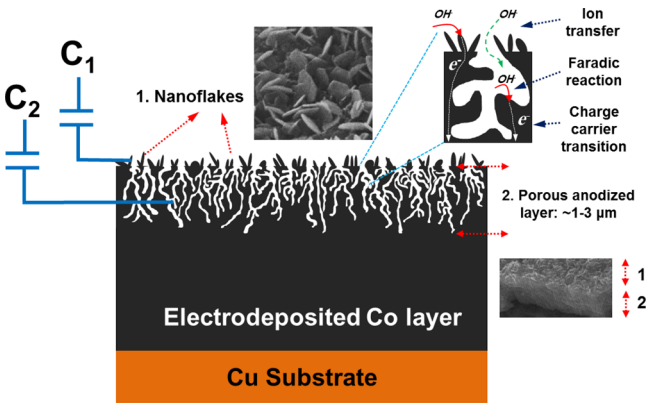

Figure 7. Schematic representation of the chemical reactions and charge carrier processes of cobalt oxide/hydroxide nanoflakes on anodized layer. Regions: (1) Nanoflakes and (2) ordered anodized layer. The C_i is the electrochemical capacitance of each layer.

diffusion process (see Supporting Information). (4) The porosity of the prepared samples did not have any limiting effect on the diffusion processes and the reactions are surface controlled. (5) The porosity of the anodized layers was homogeneous. Hence, the current, i, as a function of the potential is given by Butler−Volmer equation[51]

$$i = i_0[e^{\alpha_a \beta F\eta/RT} - e^{-\alpha_c \beta F\eta/RT}] \quad (8)$$

where i_0, η, β, F, R, and T are the exchange current, activation overpotential (V), number of electrons involved in the electrode reaction, Faraday constant (96485 C mol^{-1}), universal gas constant (8.31 J mol^{-1} K^{-1}), and temperature (K), respectively. α_a and α_c are anodic and cathodic charge transfer coefficients. By dividing the total effective surface area of the prepared electrodes into two regions, (1) nanoflakes and (2) ordered anodized layer (Figure 7), we can consider the overall current of the electrode as following:

$$i = i_1 + i_2 \quad (9)$$

On the other hand, total specific capacitance of the electrode, $C_A^{total}(\nu)$, has a linear relation to total current and i is proportion to electrochemical active sites (ν is the scan rate in CV tests). Therefore, $C_A^{total}(\nu)$ can be written as a summation function of total electrochemical active sites (s_i) of each part

$$C_A^{total}(\nu) = \sum_i s_i = K_1(\nu)A_1^{eff} + K_2(\nu)V_2 \quad (10)$$

where $K_1(\nu)$ and $K_2(\nu)$ are coefficients that indicate the weight factor of each region involved in total electrochemical capacitance as a function of scan rate (Figure 7). These parameters will be calculated by initial inputs from experimental results. These weights are parameters were substituted for unknown quantity e.g. porosity of each part. The A_1^{eff} and V_2 are effective surface area of the region 1 and volume of the region 2, and they can be written in terms of quantities that obtained from our SEM images. A_1^{eff} is proportional to outer surface area of nanoflake region and thus flake density can be written as $A_1^{eff} = nS\ (\pi(d/2)^2 + 1/2\pi\ d\ w)$. In the model, we considered a semicircular shape for all the nanoflakes and each of them had two lateral surfaces. The quantity S = 0.25 cm^2 is the total geometric surface area of the samples. V_2 is proportional the amount of matter which was anodized or the thickness of anodized layer: $V_2 = S\ l$. Hence, the total capacitance of the

DOI: 10.1021/acsami.5b00806
ACS Appl. Mater. Interfaces 2015, 7, 11172−11179

proposed model was considered by gathering together the following equation:

$$C_A^{total}(\nu) = K_1(\nu)nS\left(\frac{\pi}{4}d^2 + \frac{\pi}{2}dw\right) + K_2(\nu)Sl \quad (11)$$

By inserting the initial inputs, the weight factor, we determined $K_1(\nu)$ and $K_2(\nu)$ at each scan rate. For example, at scan rate of 2 mV s^{-1}, (I) $l = 0$ and C_A^{total} (2) = 44 mF cm^{-2} at $V = 0$ (non-anodized sample), $K_1(\nu)$ was calculated, and at (II) $n = 0$, $C_A^{total}(2)$ = 229 mF cm^{-2} at V = 50 V, and therefore, $K_2(\nu)$ was obtained. Figure 8a showed that power-law behavior was observed with exponents: −0.1 and −0.3 for $K_1(\nu)$ and $K_2(\nu)$, respectively.

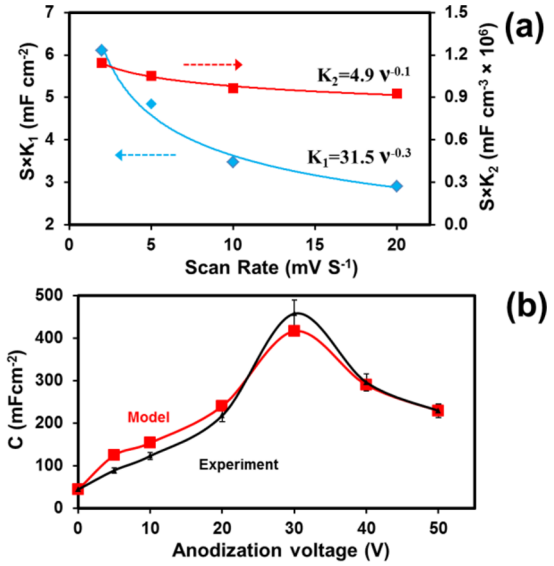

Figure 8. (a) Coefficient K_1 and K_2 (both multiplied by geometric surface area) plotted as a function of scan rate. (b) The modeled and experimental capacitance as a function of applied anodization voltages at scan rate of 2 mV s^{-1}.

To evaluate the model, at scan rate of 2 mV s^{-1}, the modeled capacitance and the measured experiment data for each applied voltage were plotted and the results are shown in Figure 8b. The behavior of the modeled capacitance was completely consistent with experimental data especially at higher anodization voltage. It is obvious that the contribution of the anodized layer was more pronounced than the nanoflakes in supercapacitance amount (because the ratio $K_2/K_1 \gg 1$ cm^{-1}). Therefore, a thicker porous Co oxide/hydroxide can be more effective than other facial nanostructures in supercapacitance applications. Of course, the ordered nanosheets (e.g., with micrometer length in size or higher d) can be competing with porous structures because of their large surface area.[13,18] In addition, the authors propose that the effect of porosity can be applied in the above equation (eq 11) as a correction factor for modifying the model.

5. CONCLUSIONS

In summary, metal cobalt layers had been electrodeposited on copper substrates. These prepared layers were anodized at different applied voltage to form cobalt oxide/hydroxide nanoflakes on top of the porous layers. The thickness of porous layers and shape and density of nanoflakes were tuned and investigated by SEM images resulted in determination of optimized electrode formed at 30 V anodization voltage (V_{anod}^{30V}) with maximum surface area (or higher active mass density of about 2 mg cm^{-2}). The XPS analysis revealed that by increasing anodization applied voltage, the surface chemical composition had also shifted to cobalt hydroxide phase. The maximum electrochemical capacitance was calculated based on analysis of CV curves and resulted in supercapacitance of 601 mF cm^{-2} at scan rate 2 mV s^{-1} for the V_{anod}^{30V} electrode. The effect of anodization voltage on formation of $Co_3O_4/Co(OH)_2$ electrode was modeled and found that the contribution of porous layer was more decisive than nanoflakes structure in supercapacitance application. Finally, the prepared nanostructured cobalt oxide/hydroxide electrode can be introduced as a low price and highly stable supercapacitor in energy storage realm.

■ ASSOCIATED CONTENT

Supporting Information

Table of highly cited published works on cobalt oxide/hydroxide electrodes synthesized by different methods, SEM images, galvanostat charge/discharge curve, XPS spectra and also calculation of the diffusion time scale of OH^- ions in the electrolyte, and field-assisted drift time scale of charge carriers through the solid phase. The Supporting Information is available free of charge on the ACS Publications website at DOI: 10.1021/acsami.5b00806.

■ AUTHOR INFORMATION

Corresponding Author

*Phone: (+98)-21-6616-4516. Fax: (+98)-21-6601-2983. E-mail: moshfegh@sharif.edu.

Notes

The authors declare no competing financial interest.

■ ACKNOWLEDGMENTS

The authors would like to thank the Research and Technology Council of Sharif University of Technology for financial support.

■ REFERENCES

(1) Li, Z.; Luo, W.; Zhang, M.; Feng, J.; Zou, Z. Photoelectrochemical Cells for Solar Hydrogen Production: Current State of Promising Photoelectrodes, Methods to Improve Their Properties, and Outlook. *Energy Environ. Sci.* **2013**, *6*, 347−370.

(2) Qorbani, M.; Naseri, N.; Moradlou, O.; Azimirad, R.; Moshfegh, A. Z. How CdS Nanoparticles Can Influence TiO_2 Nanotube Arrays in Solar Energy Applications? *Appl. Catal., B* **2015**, *162*, 210−216.

(3) Atwater, H. A.; Polman, A. Plasmonics for Improved Photovoltaic Devices. *Nat. Mater.* **2010**, *9*, 205−213.

(4) Xiao, Z.; Bi, C.; Shao, Y.; Dong, Q.; Wang, Q.; Yuan, Y.; Wang, C.; Gao, Y.; Huang, J. Efficient, High Yield Perovskite Photovoltaic Devices Grown by Interdiffusion of Solution-Processed Precursor Stacking Layers. *Energy Environ. Sci.* **2014**, *7*, 2619−2623.

(5) Wu, H.; Yu, G.; Pan, L.; Liu, N.; McDowell, M. T.; Bao, Z.; Cui, Y. Stable Li-Ion Battery Anodes by In-Situ Polymerization of Conducting Hydrogel to Conformally Coat Silicon Nanoparticles. *Nat. Commun.* **2013**, *4*, 1943.

(6) Zinth, V.; von Lüders, C.; Hofmann, M.; Hattendorff, J.; Buchberger, I.; Erhard, S.; Rebelo-Kornmeier, J.; Jossen, A.; Gilles, R. Lithium Plating in Lithium-Ion Batteries at Sub-ambient Temperatures Investigated by In-Situ Neutron Diffraction. *J. Power Sources* **2014**, *271*, 152−159.

DOI: 10.1021/acsami.5b00806
ACS Appl. Mater. Interfaces 2015, 7, 11172−11179

(7) Wang, G.; Zhang, L.; Zhang, J. A Review of Electrode Materials for Electrochemical Supercapacitors. *Chem. Soc. Rev.* **2012**, *41*, 797−828.
(8) Xiong, G.; Meng, C.; Reifenberger, R. G.; Irazoqui, P. P.; Fisher, T. S. A Review of Graphene-Based Electrochemical Microsupercapacitors. *Electroanalysis* **2014**, *26*, 30−51.
(9) Augustyn, V.; Simon, P.; Dunn, B. Pseudocapacitive Oxide Materials for High-Rate Electrochemical Energy Storage. *Energy Environ. Sci.* **2014**, *7*, 1597−1614.
(10) Li, Z.; Wang, J.; Niu, L.; Sun, J.; Gong, P.; Hong, W.; Ma, L.; Yang, S. Rapid Synthesis of Graphene/Cobalt Hydroxide Composite with Enhanced Electrochemical Performance for Supercapacitors. *J. Power Sources* **2014**, *245*, 224−231.
(11) Yan, J.; Wang, Q.; Wei, T.; Fan, Z. Recent Advances in Design and Fabrication of Electrochemical Supercapacitors with High Energy Densities. *Adv. Energy Mater.* **2014**, *4*, 1300816.
(12) Tai Dam, D.; Lee, J.-M. Ultrahigh Pseudocapacitance of Mesoporous Ni-Doped $Co(OH)_2$/ITO Nanowires. *Nano Energy* **2013**, *2*, 1186−1196.
(13) Yang, Q.; Lu, Z.; Sun, X.; Liu, J. Ultrathin Co_3O_4 Nanosheet Arrays with High Supercapacitive Performance. *Sci. Rep.* **2013**, *3*, 3537.
(14) Hercule, K. M.; Wei, Q.; Khan, A. M.; Zhao, Y.; Tian, X.; Mai, L. Synergistic Effect of Hierarchical Nanostructured $MoO_2/Co(OH)_2$ with Largely Enhanced Pseudocapacitor Cyclability. *Nano Lett.* **2013**, *13*, 5685−5691.
(15) Ryu, I.; Yang, M.; Kwon, H.; Park, H. K.; Do, Y. R.; Lee, S. B.; Yim, S. Coaxial RuO_2−ITO Nanopillars for Transparent Supercapacitor Application. *Langmuir* **2014**, *30*, 1704−1709.
(16) Liu, Y.; Yan, D.; Li, Y.; Wu, Z.; Zhuo, R.; Li, S.; Feng, J.; Wang, J.; Yan, P.; Geng, Z. Manganese Dioxide Nanosheet Arrays Grown on Graphene Oxide as an Advanced Electrode Material for Supercapacitors. *Electrochim. Acta* **2014**, *117*, 528−533.
(17) Xiong, G.; Hembram, K. P. S. S.; Reifenberger, R. G.; Fisher, T. S. MnO_2-Coated Graphitic Petals for Supercapacitor Electrodes. *J. Power Sources* **2013**, *227*, 254−259.
(18) Rakhi, R. B.; Chen, W.; Hedhili, M. N.; Cha, D.; Alshareef, H. N. Enhanced Rate Performance of Mesoporous Co_3O_4 Nanosheet Supercapacitor Electrodes by Hydrous RuO_2 Nanoparticle Decoration. *ACS Appl. Mater. Interfaces* **2014**, *6*, 4196−4206.
(19) Xue, T.; Lee, J.-M. Capacitive Behavior of Mesoporous $Co(OH)_2$ Nanowires. *J. Power Sources* **2014**, *245*, 194−202.
(20) Dam, D. T.; Lee, J.-M. Three-Dimensional Cobalt Oxide Microstructures with Brush-like Morphology via Surfactant-Dependent Assembly. *ACS Appl. Mater. Interfaces* **2014**, *6*, 20729−20737.
(21) Wang, D.-W.; Li, F.; Cheng, H.-M. Hierarchical Porous Nickel Oxide and Carbon as Electrode Materials for Asymmetric Supercapacitor. *J. Power Sources* **2008**, *185*, 1563−1568.
(22) Xiong, X.; Ding, D.; Chen, D.; Waller, G.; Bu, Y.; Wang, Z.; Liu, M. Three-Dimensional Ultrathin $Ni(OH)_2$ Nanosheets Grown on Nickel Foam for High-Performance Supercapacitors. *Nano Energy* **2015**, *11*, 154−161.
(23) Ma, X.; Li, Y.; Wen, Z.; Gao, F.; Liang, C.; Che, R. Ultrathin β-$Ni(OH)_2$ Nanoplates Vertically Grown on Nickel-Coated Carbon Nanotubes as High-Performance Pseudocapacitor Electrode Materials. *ACS Appl. Mater. Interfaces* **2014**, *7*, 974−979.
(24) Chen, L.-F.; Yu, Z.-Y.; Wang, J.-J.; Li, Q.-X.; Tan, Z.-Q.; Zhu, Y.-W.; Yu, S.-H. Metal-Like Fluorine-Doped β-FeOOH Nanorods Grown on Carbon Cloth for Scalable High-Performance Supercapacitors. *Nano Energy* **2015**, *11*, 119−128.
(25) Mohamed, S. G.; Chen, C.-J.; Chen, C. K.; Hu, S.-F.; Liu, R.-S. High-Performance Lithium-Ion Battery and Symmetric Supercapacitors Based on $FeCo_2O_4$ Nanoflakes Electrodes. *ACS Appl. Mater. Interfaces* **2014**, *6*, 22701−22708.
(26) Wang, Q.; Wang, X.; Xu, J.; Ouyang, X.; Hou, X.; Chen, D.; Wang, R.; Shen, G. Flexible Coaxial-Type Fiber Supercapacitor Based on $NiCo_2O_4$ Nanosheets Electrodes. *Nano Energy* **2014**, *8*, 44−51.
(27) Ghosh, D.; Das, C. K. Hydrothermal Growth of Hierarchical Ni_3S_2 and Co_3S_4 on a Reduced Graphene Oxide Hydrogel@Ni Foam: A High-Energy-Density Aqueous Asymmetric Supercapacitor. *ACS Appl. Mater. Interfaces* **2014**, *7*, 1122−1131.
(28) Hu, W.; Chen, R.; Xie, W.; Zou, L.; Qin, N.; Bao, D. $CoNi_2S_4$ Nanosheet Arrays Supported on Nickel Foams with Ultrahigh Capacitance for Aqueous Asymmetric Supercapacitor Applications. *ACS Appl. Mater. Interfaces* **2014**, *6*, 19318−19326.
(29) Lokhande, C. D.; Dubal, D. P.; Joo, O.-S. Metal Oxide Thin Film Based Supercapacitors. *Curr. Appl. Phys.* **2011**, *11*, 255−270.
(30) Chen, Z.; Chen, Y.; Zuo, C.; Zhou, S.; Xiao, A. G.; Pan, A. X. Hydrothermal Synthesis of Porous $Co(OH)_2$ Nanoflake Array Film and Its Supercapacitor Application. *Bull. Mater. Sci.* **2013**, *36*, 239−244.
(31) Wang, H.; Qing, C.; Guo, J.; Aref, A. A.; Sun, D.; Wang, B.; Tang, Y. Highly Conductive Carbon-CoO Hybrid Nanostructure Arrays with Enhanced Electrochemical Performance for Asymmetric Supercapacitors. *J. Mater. Chem. A* **2014**, *2*, 11776−11783.
(32) Xia, X.-h.; Tu, J.-p.; Zhang, Y.-q.; Mai, Y.-j.; Wang, X.-l.; Gu, C.-d.; Zhao, X.-b. Freestanding Co_3O_4 Nanowire Array for High Performance Supercapacitors. *RSC Adv.* **2012**, *2*, 1835−1841.
(33) Ban, S.; Zhang, J.; Zhang, L.; Tsay, K.; Song, D.; Zou, X. Charging and Discharging Electrochemical Supercapacitors in the Presence of Both Parallel Leakage Process and Electrochemical Decomposition of Solvent. *Electrochim. Acta* **2013**, *90*, 542−549.
(34) Somasundaram, K.; Birgersson, E.; Mujumdar, A. S. Analysis of a Model for an Electrochemical Capacitor. *J. Electrochem. Soc.* **2011**, *158*, A1220−A1230.
(35) Subramanian, V. R.; Devan, S.; White, R. E. An Approximate Solution for a Pseudocapacitor. *J. Power Sources* **2004**, *135*, 361−367.
(36) Ike, I. S.; Sigalas, I.; Iyuke, S.; Ozoemena, K. I. An Overview of Mathematical Modeling of Electrochemical Supercapacitors/Ultracapacitors. *J. Power Sources* **2015**, *273*, 264−277.
(37) Lee, C.-Y.; Lee, K.; Schmuki, P. Anodic Formation of Self-Organized Cobalt Oxide Nanoporous Layers. *Angew. Chem., Int. Ed.* **2013**, *52*, 2077−2081.
(38) Xia, X.-h.; Tu, J.-p.; Mai, Y.-j.; Wang, X.-l.; Gu, C.-d.; Zhao, X.-b. Self-Supported Hydrothermal Synthesized Hollow Co_3O_4 Nanowire Arrays with High Supercapacitor Capacitance. *J. Mater. Chem.* **2011**, *21*, 9319−9325.
(39) Gao, Y. Y.; Chen, S. L.; Cao, D. X.; Wang, G. L.; Yin, J. L. Electrochemical Capacitance of Co_3O_4 Nanowire Arrays Supported on Nickel Foam. *J. Power Sources* **2010**, *195*, 1757−1760.
(40) Gong, D.; Grimes, C. A.; Varghese, O. K.; Hu, W. C.; Singh, R. S.; Chen, Z.; Dickey, E. C. Titanium Oxide Nanotube Arrays Prepared by Anodic Oxidation. *J. Mater. Res.* **2001**, *16*, 3331−3334.
(41) Rani, S.; Roy, S. C.; Paulose, M.; Varghese, O. K.; Mor, G. K.; Kim, S.; Yoriya, S.; LaTempa, T. J.; Grimes, C. A. Synthesis and Applications of Electrochemically Self-Assembled Titania Nanotube Arrays. *Phys. Chem. Chem. Phys.* **2010**, *12*, 2780−2800.
(42) Hosono, E.; Fujihara, S.; Honma, I.; Ichihara, M.; Zhou, H. Synthesis of the CoOOH Fine Nanoflake Film with the High Rate Capacitance Property. *J. Power Sources* **2006**, *158*, 779−783.
(43) Roy, P.; Berger, S.; Schmuki, P. TiO_2 Nanotubes: Synthesis and Applications. *Angew. Chem., Int. Ed.* **2011**, *50*, 2904−2939.
(44) Kong, L.-B.; Lang, J.-W.; Liu, M.; Luo, Y.-C.; Kang, L. Facile Approach to Prepare Loose-Packed Cobalt Hydroxide Nano-Flakes Materials for Electrochemical Capacitors. *J. Power Sources* **2009**, *194*, 1194−1201.
(45) Yang, J.; Walczak, K.; Anzenberg, E.; Toma, F. M.; Yuan, G.; Beeman, J.; Schwartzberg, A.; Lin, Y.; Hettick, M.; Javey, A.; Ager, J. W.; Yano, J.; Frei, H.; Sharp, I. D. Efficient and Sustained Photoelectrochemical Water Oxidation by Cobalt Oxide/Silicon Photoanodes with Nanotextured Interfaces. *J. Am. Chem. Soc.* **2014**, *136*, 6191−6194.
(46) Liao, L.; Zhang, Q.; Su, Z.; Zhao, Z.; Wang, Y.; Li, Y.; Lu, X.; Wei, D.; Feng, G.; Yu, Q.; Cai, X.; Zhao, J.; Ren, Z.; Fang, H.; Robles-Hernandez, F.; Baldelli, S.; Bao, J. Efficient Solar Water-Splitting Using a Nanocrystalline CoO Photocatalyst. *Nat. Nano.* **2014**, *9*, 69−73.
(47) Zhang, Z.; Hao, J.; Yang, W.; Lu, B.; Ke, X.; Zhang, B.; Tang, J. Porous Co_3O_4 Nanorods—Reduced Graphene Oxide with Intrinsic

DOI: 10.1021/acsami.5b00806
ACS Appl. Mater. Interfaces 2015, 7, 11172−11179

Peroxidase-Like Activity and Catalysis in the Degradation of Methylene Blue. *ACS Appl. Mater. Interfaces* **2013**, *5*, 3809−3815.
(48) Spataru, N.; Terashima, C.; Tokuhiro, K.; Sutanto, I.; Tryk, D. A.; Park, S.-M.; Fujishima, A. Electrochemical Behavior of Cobalt Oxide Films Deposited at Conductive Diamond Electrodes. *J. Electrochem. Soc.* **2003**, *150*, E337−E341.
(49) Behazin, M.; Biesinger, M. C.; Noël, J. J.; Wren, J. C. Comparative Study of Film Formation on High-Purity Co and Stellite-6: Probing the Roles of a Chromium Oxide Layer and Gamma-Radiation. *Corros. Sci.* **2012**, *63*, 40−50.
(50) Jiang, J.; Liu, J.; Ding, R.; Zhu, J.; Li, Y.; Hu, A.; Li, X.; Huang, X. Large-Scale Uniform α-$Co(OH)_2$ Long Nanowire Arrays Grown on Graphite as Pseudocapacitor Electrodes. *ACS Appl. Mater. Interfaces* **2010**, *3*, 99−103.
(51) Bard, A. J.; Faulkner, L. R. *Electrochemical Methods: Fundamentals and Applications*; Wiley: New York, 2000; Chapter 3, pp 87−136.
(52) Li, N.; Xu, J.-Z.; Yao, H.; Zhu, J.-J.; Chen, H.-Y. The Direct Electron Transfer of Myoglobin Based on the Electron Tunneling in Proteins. *J. Phys. Chem. B* **2006**, *110*, 11561−11565.
(53) Rakhi, R. B.; Chen, W.; Cha, D.; Alshareef, H. N. Substrate Dependent Self-Organization of Mesoporous Cobalt Oxide Nanowires with Remarkable Pseudocapacitance. *Nano Lett.* **2012**, *12*, 2559−2567.
(54) Gogotsi, Y.; Simon, P. True Performance Metrics in Electrochemical Energy Storage. *Science* **2011**, *334*, 917−918.
(55) Mondal, C.; Ganguly, M.; Manna, P. K.; Yusuf, S. M.; Pal, T. Fabrication of Porous β-$Co(OH)_2$ Architecture at Room Temperature: A High Performance Supercapacitor. *Langmuir* **2013**, *29*, 9179−9187.

DOI: 10.1021/acsami.5b00806
ACS Appl. Mater. Interfaces 2015, 7, 11172−11179